

MFIG — A Mass Filtered Ion Gauge

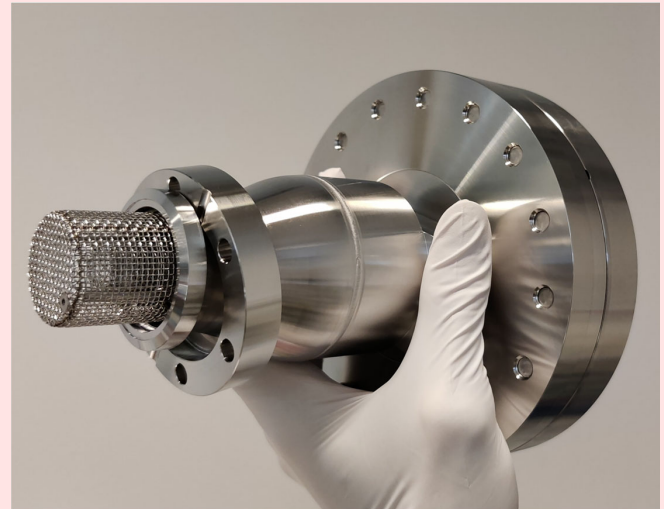
Herman Bekman,[†] Jurjen Emmelkamp, Youyou Westland, Dorus Elstgeest, Thomas Mechielsen, Michael Haye, Freek Molkenboer, Norbert Koster, Henk Lensen

Department Nano Instrumentation, TNO, Stieltjesweg 1, NL 2628 CK Delft, The Netherlands

[†] Corresponding author: herman.bekman@tno.nl

Received: 18 November, 2022; Accepted: 23 July, 2023; J-STAGE Advance Publication: 7 September, 2023; Published: 7 September, 2023

This paper describes a new version of the mass filtered ion gauge (MFIG) sensor [D. Maas *et al.*, Proc. SPIE **10145**, 101452I (2017)]. By changing the entire design of the sensor its sensitivity could be improved, its mass filter function could be improved and last but not least its electronics was made far more robust. MFIG (shown in Graphical Abstract) is a metrology tool for detecting low levels of contamination (volatile organic compounds) with a high time resolution. As such it detects bursts, but also transients and continuous contamination in high vacuum systems. The high time resolution for an extended mass range discriminates this sensor from a residual gas analyzer (RGA). MFIG is also more sensitive than a state-of-the-art RGA as a result you can also detect contamination earlier. As such the MFIG sensor can be used as a traffic light and it can alert the system or operator in an early state when the system is out-of-spec. With these two unique characteristics the MFIG can prevent additional contamination to the system or additional yield loss. The development of this sensor was done within the European program MadeIn4. The development started with a use case and requirement analysis. The design process was supported by COMSOL™ modeling. After realization of MFIG sensor it was evaluated in a laboratory environment in which we could insert controlled gas mixture into a high vacuum system. In this paper we will show that MFIG is both more sensitive and faster than a state-of-the-art RGA in detecting contaminations.



Keywords Residual gas analyzer; Contamination sensor; Ion beam modelling

I. INTRODUCTION

A mass filtered ion gauge (MFIG, Figure 1) [1] is a metrology tool for detecting low levels of contamination [volatile organic compounds (VOC) and airborne molecular contamination (AMC)]. MFIG can detect “short” bursts (1 s time resolution) of contamination starting from a selectable mass. The selectivity of the MFIG sensor is defined as the lower mass (50% transmission) of the mass range for which MFIG is sensitive. The selectivity can be tuned by an electrostatic lens. When contamination bursts have been detected the operator or the system can immediately be notified and either the operator or the system can take appropriate actions, allowing for cycle-time reduction in case of a contamination event and thus enhancing productivity/yield.

MFIG consist of an ion source followed by an electrostatic

lens for beam focus control. After the electrostatic lens mass separation is achieved with a static magnet field. Detection is done by a Faraday cup.

In this paper, we will compare MFIG to the quadrupole residual gas analyzer (RGA), since that is the most common RGA used in the field. We are aware that other types of mass spectrometer systems are invented, like the Mattauch-Herzog sensor or the ion-trap mass analyzers, which all will compare differently to MFIG.

A. Use cases for MFIG

Detecting short bursts and transients is a key factor of MFIG coupled to time resolution. Because MFIG is also more sensitive than a state-of-the-art RGA, you can also detect contamination earlier. Based on these characteristics several use cases of MFIG are identified for usage in a high-

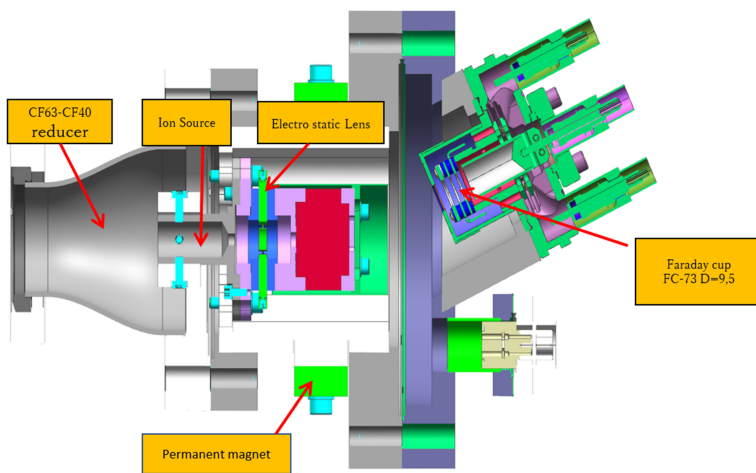


Figure 1: CAD cross-cut through MFIG. Since a standard RGA typically come with a CF40 flange we wanted to stick to this flange size. As MFIG does not fit in a CF40 tube, we needed a CF63-to-CF40 reducer for connection of MFIG to a CF40 port.

vacuum system, (pressure $<10^{-6}$ mbar). These use cases are discussed in more detail in the following paragraphs.

1. Monitoring contamination molecules in a high-vacuum system

The MFIG sensor is installed on a vacuum system that is sensitive to contamination, either for the vacuum system itself or the product/samples that are loaded. MFIG can detect volatile contaminants and act as a warning system. When the contamination detection signal raises above a user defined threshold value a warning signal will be generated, and the product/samples can be ejected immediately preventing further yield loss.

2. High-vacuum gauge with MFIG

In this use-case, the MFIG sensor combines the function of a contamination sensor, measuring the partial pressure of a specific mass range with a high vacuum gauge, measuring the total pressure in the high vacuum system. It is expected in this use-case that the MFIG sensor is mainly used as a high vacuum gauge, and when desired will measure only a specific mass range.

Combining the partial pressure of a specific mass range with the total pressure will lead to a continuous measurement of the gas fraction of the specific mass range.

3. Monitoring outgassing rates

In this use-case, the MFIG sensor is used to measure several specific mass ranges in a high vacuum system for the qualification of outgassing of products/materials to be used in vacuum systems during system development and fabrication/test.

4. Evaluation use cases

We evaluated the use cases from a supplier and a buyer perspective. We have selected the use case: "monitoring contamination molecules in a high vacuum system", as we found it the most attractive use case. In the design of MFIG

we therefore focussed on improving the MFIG performance for this specific use-case. For this purpose, we performed an extensive modelling study using COMSOL™.

II. MODELLING

The modelling focused on two different aspects of the MFIG:

1. Ion source modelling for selecting the most appropriate ion source to drive the MFIG;
2. MFIG design modelling to achieve the best contamination detection with respect to signal to noise ratio and selectivity.

A. Ion source modelling

For the MFIG system, we need to select a commercial electron-impact ion source, usually used for RGA. We modelled two of these ion sources, but with a different cathode set-up, and based on the analytical and simulation modelling results we selected the most appropriate electron-impact RGA ion source for the MFIG sensor.

For optimal MFIG performance the ion source should meet the following selection criteria:

1. Ion energy homogeneity for improved selectivity;
2. Ion flux at 1×10^{-6} – 1×10^{-8} mbar for achieving higher signal-to-noise ratios (SNR);
3. Cross-section size and shape of the ion beam for optimal electrostatic focusing and magnetic beam deflection.

The ionization rate is calculated analytically and is used as input for the simulation modelling. The ion source modelling is only discussed briefly, and a full description of the ion source modelling is to be published soon.

1. Ion sources simulated

Two electron impact ion sources are selected, with two different filament set-ups. The first source is the RGA source of Stanford Research Systems (SRS) and referred to as an SRS ion source. This SRS source uses a circular filament,



Figure 2: SRS RGA ion source, with the circular filament around the wired anode cage. The ion outlet is in the bottom plate. The repeller cage has been removed for photographic reasons. For the Hiden Analytical RGA ion source, we refer to the company's website [2]. The main difference between the SRS and Hiden Analytical ion sources is the placement of the filaments. In contrast with the SRS ion source, the Hiden source uses two longitudinal filaments placed parallel to the anode cage.

positioned around the anode cage, which is in contrast with the other selected RGA source, equipped with two parallel longitudinally placed filaments next to the anode cage. This ion source is manufactured by Hiden Analytical and is referred to as a Hiden ion source. The SRS source is shown in Figure 2. The Hiden source can be found at the website of Hiden Analytical [2]. Although both sources have identical working principles, the different filament orientations of the sources result in different ion-beam properties. The dimensions of the SRS source have been measured at an actual source, the dimensions of the Hiden source have been estimated based on the schematic drawing. We have taken the open version of the Hiden source, with a wired outer cage. Since we did not have the actual dimensions of the Hiden source small deviations between the simulation results and the actual ion beam properties could apply, however, since we focus on the effect of the filament orientations, we expect that these deviations are negligible.

B. General working principle of an electron-impact ion source

In the electron-impact ion source, the electrons are emitted from a heated filament cathode by thermionic emission. These filaments are placed in the electrical field between grounded repeller cage and the positive anode cage, and therefore the electrons are accelerated towards the anode, see Figure 3. Due to its open structure, the electrons can pass the anode grid and are reversed once passed the anode by the opposite pointed electric field. These oscillations continue until the electrons are collected by the wires of the anode cage.

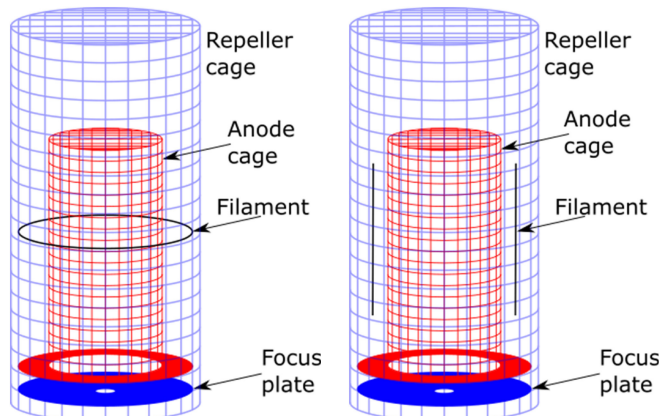


Figure 3: Schematic of the ion sources. Blue: grounded; Red: positive anode voltage; Black: positive intermediate cathode voltage. Left: SRS ionizer with circular filament. Right: Hiden ionizer with two parallel longitudinal filaments, based on Ref. 2.

In case of a collision between electron and gas molecule positive ionization can occur. The ion beam is formed by ions being accelerated towards the grounded outlet of the ion source by the internal electrical field in the anode cage. The applied ion energy is equal to the electric potential at the ionization site multiplied by the charge of the ion ($+1e$).

1. Thermionic electron emission

Hot cathode emission or thermionic emission is the emission of electrons from a material based on the $k_B T$ energy of the electrons, and the electron flux can be written as [3]:

$$J(T, W) = \lambda_R A_R T^2 e^{-\frac{W}{k_B T}},$$

where k_B is the Boltzmann constant, J is the emission current density, as a function of T (absolute temperature) and W (work function of the filament surface material), λ_R is the material-specific correlation factor, typically 0.5, and A_R is Richardson's constant, equal to $1.20 \times 10^6 \text{ A m}^{-2} \text{ K}^{-2}$ [4]. The Hiden ion source comes standard with burnout-resistant oxide coated iridium filaments, with a work function of 4.2 eV [5]. The SRS ion source comes with thoria-coated iridium. Based on the filament dimensions and the working temperature of 1673 K [6], we calculated the work function at 3.5 eV, which is in agreement with typical work functions for metallic materials [7]. Similarly, the working temperature of the Hiden source was calculated at 2007 K.

2. Ionization rate

The ionization rate J_{ion} is calculated based on the cathodic electron emission current I_{em} and the elementary charge e of the electron, the average number of electrons passing the anode cage N_{pass} , based on the open fractions of the anode cage, the diameter of the anode cage $\varnothing_{\text{anode}}$ and the electron-neutral mean free path λ_{en} :

$$J_{\text{ion}} = \frac{I_{\text{em}}}{e} N_{\text{pass}} \frac{\varnothing_{\text{anode}}}{\lambda_{\text{en}}}.$$

The electron-neutral mean free path can be calculated as [8]:

$$\lambda_{en} = \frac{k_B T}{\sigma_{eM} p_M}.$$

σ_{eM} is the ionization cross section of a gas with molar mass M and p_M the partial pressure of the related gas. Ionization cross sections of several common gases are shown in Figure 4. N_{pass} is estimated on the wire fraction (f_{wire}) of the anode cage:

$$N_{pass} = \sum_{i=1}^{\infty} [(1 - f_{wire})^2]^{2i-1}.$$

The SRS anode cage was used to estimate the open fraction of the anode. The wire diameters were measured at 0.4 mm, and with measured wire spaces (edge-edge) of 1.2 mm, the open fraction was 56%, resulting in $N_{pass} = 0.82$. The Hiden anode cage was not measured, and therefore we estimated the Hiden N_{pass} value equal to the SRS value at 0.82.

The ionization cross section of contaminants with mass M is estimated to the ionization cross section and molar mass of xenon by the equation proposed:

$$\sigma_M \sim \sigma_{Xe} \left(\frac{M_M}{M_{Xe}} \right)^{2/3},$$

where $\sigma_{Xe} = 5.41 \times 10^{-20} \text{ m}^2$ ($E = 70 \text{ eV}$) [9] and M_{Xe} is 131.39 amu, as average over the major 9 isotopes.

C. Numerical model

A multiphysics finite element modelling (FEM) software

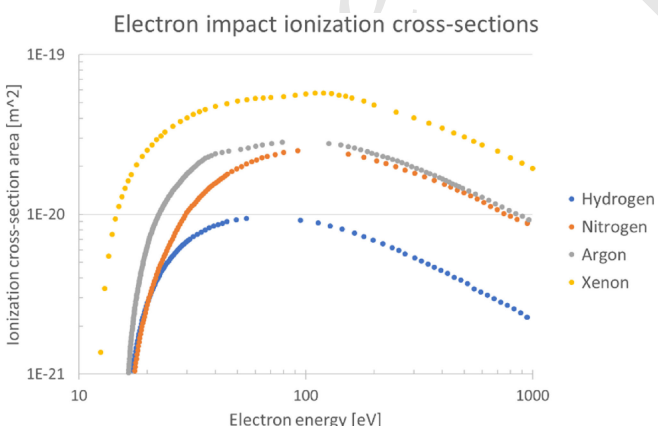


Figure 4: Calculated electron impact ionization cross-sections, obtained from Biagi database v. 8.97, LxCat [9].

Table 1: Sequence of model steps.

Step	Type	Physics	Times	Outcome
1	Analytical			Ionization rate.
2	Stationary	Electrostatics (es)		Electric potential.
3	Time dependent	Charged Particle Tracing (cpt)	range(0,10e-10,10e-8)	Electron trajectories, electron space charge density.
4	Stationary	Electrostatics (es1)		Electric potential and electron space charge density required for ion energy distribution.
5	Time dependent	Charged Particle Tracing (cpt1)	range(0,3e-6,3e-4)	Ion trajectories.

package COMSOL 6.0 was used for the simulation modelling. The electrostatics (es) and charged particle tracing (cpt) modules were coupled explicitly to simulate the electron and ion trajectories and current densities and to estimate the spatial ionization site distribution. The explicit scheme is shown in Table 1.

We have investigated the possibilities of the intrinsically more correct method of implicit coupling, however due to extremely long calculation times, this is simply not feasible for both electrons and ions in a three-dimensional (3D) model. Instead, using explicit coupling we were able to perform 3D simulations on both electrons and ions. The symmetric 3D-models of both ion sources are shown in Figure 5. The filament potential is set to 40 V and the anode is set to 110 V. The outer structure of the cylindrical ion source is grounded. The electrons travel through the anode cage with a kinetic energy of 70 eV and the ion energy is set to 110 eV. The filament emission current is set to 400 μA. The intended use of the sources is to ionize gas molecules with a molar mass of 100 g mol⁻¹ or higher. Therefore, simulations were on a gas with a molar mass of 100 g mol⁻¹.

The dimensions used for the two ion source models are listed in Table 2. The dimensions are measured at the actual source (SRS) are estimated based on the schematic drawing at the company's website (Hiden) [2].

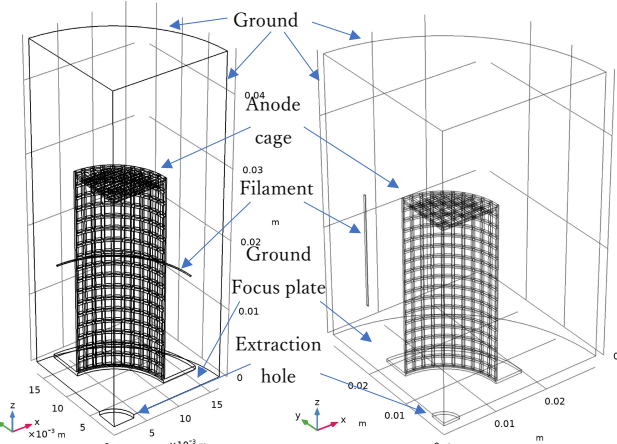
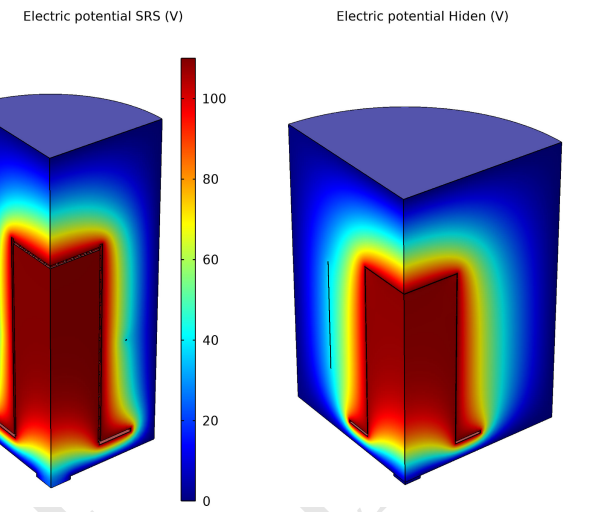


Figure 5: Models of the SRS (left) and Hiden (right) ion sources. Symmetry on $x = 0$ and $y = 0$.

1 **Table 2:** Ion source dimensions used for the simulation models. All
 2 dimensions in mm. Vertical positions in relation with focus plate.

	SRS source	Hiden source
Repeller diameter	32.7	63
Repeller length	45.5	47
Anode cage diameter	15	20
Anode foot plate diameter	25	16
Anode length	28	33
Anode wire diameter	0.4	0.4
Anode wire distance (edge-edge)	1.2	1.2
Anode vertical position	3.3	3.3
Filament diameter	23	
Filament length		2.3
Filament wire diameter	0.2	0.2
Filament-anode distance	4	21
Filament vertical position	14	10
Extraction hole diameter	6	6



17 **Figure 6:** Potential fields with anode at 110 V for SRS (left) and
 18 Hiden (right). Color scale is for both figures.
 19

20 D. Modeling results

21 The modeling results are treated according to the three ion
 22 source selection criteria.

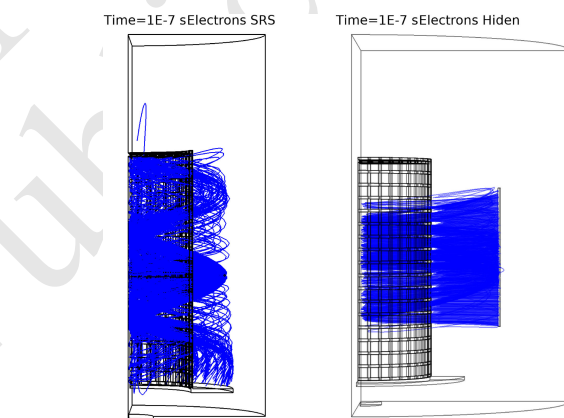
23 1. Ion source current

24 The ionization rates of both sources are calculated analytically
 25 on a gas with a molar mass of 100 g mol^{-1} , at a pressure
 26 of $3 \times 10^{-7} \text{ mbar}$ and a temperature of 300 K. The ionization
 27 cross section is estimated at $4.51 \times 10^{-20} \text{ m}^2$, based on the
 28 ionization cross section for xenon and an electron energy of
 29 70 eV. The corresponding electron mean free path is 3.06 km.
 30 Based on the larger anode diameter of the Hiden source
 31 (2.0 cm, compared to 1.5 cm for the SRS source), the Hiden
 32 source is expected to deliver a higher ion current (2.15 nA)
 33 than the SRS source (1.61 nA) in case of a gas with molar
 34 mass of 100 g mol^{-1} , at $3 \times 10^{-7} \text{ mbar}$ and 300 K, and N_{pass} at
 35 0.82.

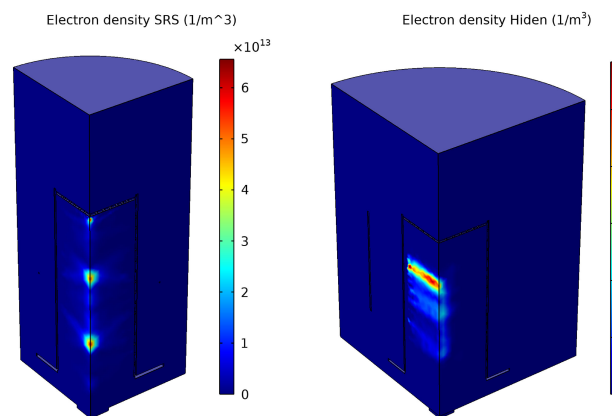
36 2. Ion energy distribution

37 The ion energy distribution is related to the distribution of
 38 ionization sites within the electric potential field inside the
 39 anode cage. Although the electric potential field is affected
 40 by the electron space charge distribution inside the anode
 41 cage, we estimate that this effect is negligible due to intrinsic
 42 compensation of the negative electron space charge by the
 43 positive ion distribution [10]. These electrical fields are
 44 shown in Figure 6. Both sources show good homogeneity
 45 of the potential field inside the anode, except for the bottom
 46 area of the anode. Therefore, ionization close to the anode
 47 bottom should be avoided.

48 The ionization site distribution is expected to be related
 49 directly to the electron space charge distribution, which can
 50 be derived using electron trajectory simulation. Electron
 51 trajectories for the ion sources are shown in Figure 7, and
 52 the accompanying electron space charge distribution is
 53 shown in Figure 8. Both sources show completely different
 54 electron trajectories, and thus space charge distributions,



33 **Figure 7:** Electron trajectories in the SRS (left) and Hiden (right)
 34 source.
 35



50 **Figure 8:** Electron space charge density inside the anode cage
 51 indicating ionization site distribution. Left: SRS. Right: Hiden.
 52

53 caused by the different filament orientations. The ionization
 54 site distribution in the Hiden source is like a vertical planar
 55 disk through the center of the anode, while the SRS source
 56 shows a wider spread ionization site distribution around three
 57

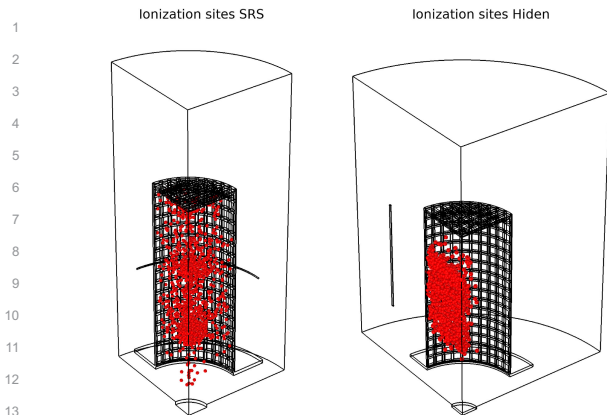


Figure 9: Ionization sites based on electron space charge density for SRS (left) and Hiden (right).

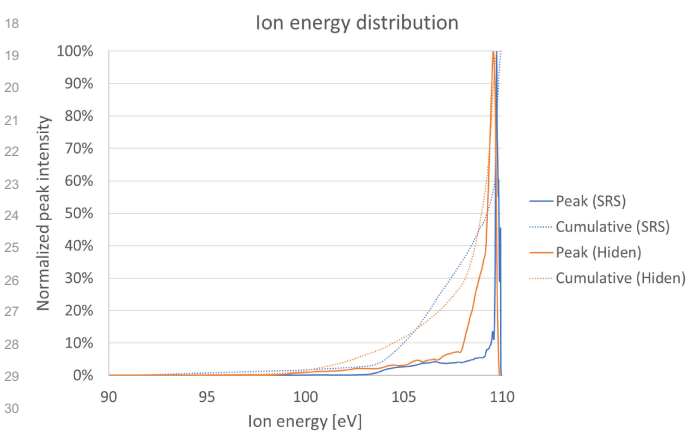


Figure 10: Ion energy distribution of the SRS (blue) and Hiden (orange) sources.

central spots along the center line of the anode (see Figure 9).

Applying histogram functions over the ionization sites and the potential field inside the anode results in the ion energy distribution. The peak and cumulative ion energy distribution of both sources is shown in Figure 10. The sources show ion energy values in the range of 100–108 eV (Hiden) and 104–109 eV (SRS), but where the Hiden source really inclines at 108 eV, the SRS remains low till 109 eV. The median ion energy is 108.9 eV for the Hiden source, and 109.25 eV for the SRS source. This results in a more homogeneous ion energy distribution in the SRS source.

3. Ion beam shape

After ionization the positive ions are accelerated towards the exit into a beam, as shown in Figure 11. Not all ions formed are collected into the beam, some get expelled from the anode cage via the grid openings. The SRS source shows an ion collection of 90.3%, while this 92.2% for the Hiden. Together with the previous calculated ionization rates, the Hiden source shows a significantly higher beam current of 1.98 nA, compared to 1.45 nA for the SRS source.

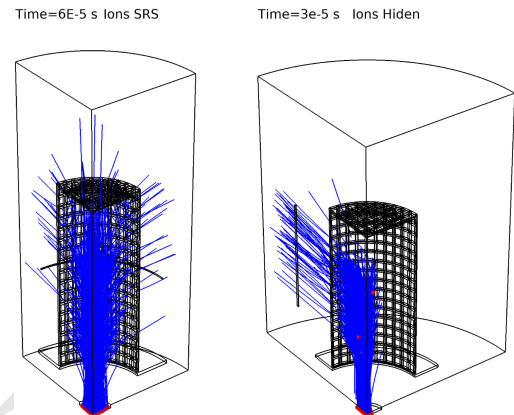


Figure 11: Ion trajectories for the SRS (Left) and Hiden (Right) source. Residence times are for 99.9% collection of ions. Due to the larger anode diameter of the Hiden source the ions experience a larger electrical field towards the extraction hole and thus are accelerated faster to the exit compared to the SRS source.

Due to the position of the ionization sites in the anode cage, both sources show different beam current densities, as shown in Figure 12. The SRS source shows a gaussian like high intensity circular beam ($J_{\max} = 0.291 \text{ mA m}^{-2}$), due to symmetric radial ionization around the center axis. On the other hand, the Hiden source has a planar ionization site distribution, translating in a flat beam profile across the beam outlet with much lower intensity ($J_{\max} = 0.111 \text{ mA m}^{-2}$).

4. Ion source selection

We selected three selection criteria: beam current, ion energy distribution, and beam shape. Although the Hiden source showed the highest beam current, the flat planar beam shape is expected to be less useful for electrostatic beam focusing and magnetic beam deflection in the MFIG. Next to that, the slightly better ion energy homogeneity of the SRS source allows better tunability of the MFIG. Overall, we expect the beam shape and the ion energy homogeneity are of higher value than the beam current itself, and therefore we selected the SRS source as ionization source for the MFIG.

E. MFIG design modelling

The MFIG system is basically a series of 4 subsystems:

- Ion source
- Electrostatic lens for ion beam focusing
- Magnetic deflector for mass separation
- Faraday cup detector

The ion source already has been described intensely in the previous chapter. The three remaining subsystems are described in this chapter, based on the optimization of the following two criteria:

- Sensitivity: increase SNR of the contaminants by suppressing the detection of low-mass ions due to scattering;
- Selectivity: improve mass cut-off function by combining ion beam focusing with magnetic deflection for mass separation.

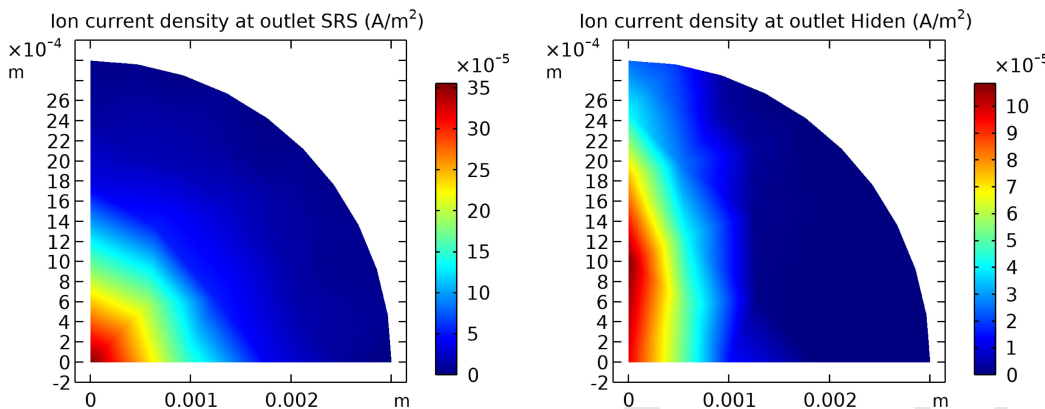


Figure 12: Ion beam current density at ion source outlet (x - y plane) for SRS (left) and Hiden (right). Due to text orientation different tick marks are used for x and y axes.

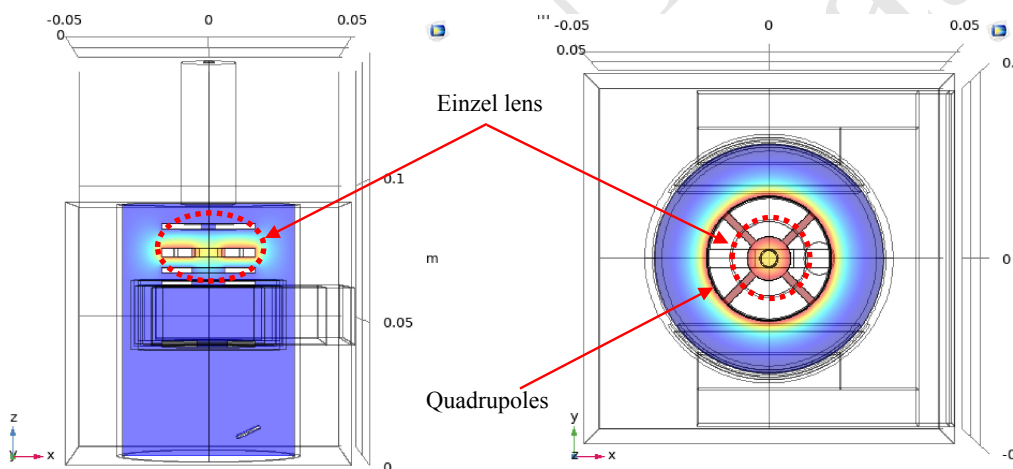


Figure 13: Electrical potential field by the Einzel lens. A voltage is set to the quadrupoles, all other structures are grounded. Left: xz -plane at $y = 0$; Right: xy -plane through the center of the E-lens. The quadrupoles are shown in white.

F. General working principle

The Mass-Filtered Ion Gauge or MFIG can detect molecular contaminants such as hydrocarbons in a vacuum environment. The MFIG contains an ion source, which is placed as a sampler inside the vacuum chamber. Ions created by this ion source, or ionizer, are accelerated out of the ionizer towards an electrical lens, which focusses the ion beam. Besides focusing the electrical lens also can deflect the ion beam for correctional purposes. After the electrical lens the ions pass a magnetic field that deflects the ion beam based on the ion masses. Lighter ions are deflected more than heavier ions, and thus discrimination of the ions based on ion mass is achieved. The ions of interest are collected inside a faraday cup, creating a current due to the charge flow at the detector. The MFIG is designed such that the ion selection is as a band filter, with a minimum and maximum detectable ion mass. Ions with masses outside the mass set-points are not collected by the detector inside the faraday cup. To suppress ions from the process gases, the minimum mass, called selection, is set above the mass of krypton, and is around 100 amu. The

maximum mass is above the molecular mass of volatile molecules at working temperatures of around 20°C and is around 400 amu.

G. Ion beam focusing by electrostatic einzel lense

To obtain optimal sensitivity and selectivity ion beam focusing at the faraday cup is required. Focusing is achieved by an electrostatic, or einzel, lens, which consists of three parts: two grounded apertures, and an aperture at a positive einzel potential in between the grounded apertures to apply the electrical field. Conventionally, the middle or einzel aperture is a monopole aperture, like the outer grounded apertures. In our case, the monopole has been replaced by a quadrupole, see Figure 13. This allows small deviations to the einzel voltage in x and y directions, which allows beam alignment corrections on top of the beam focusing.

Focusing of the ion beam is mass independent, but is not ion energy independent, and therefore, the einzel lens requires homogeneous ion energy for optimal focusing.

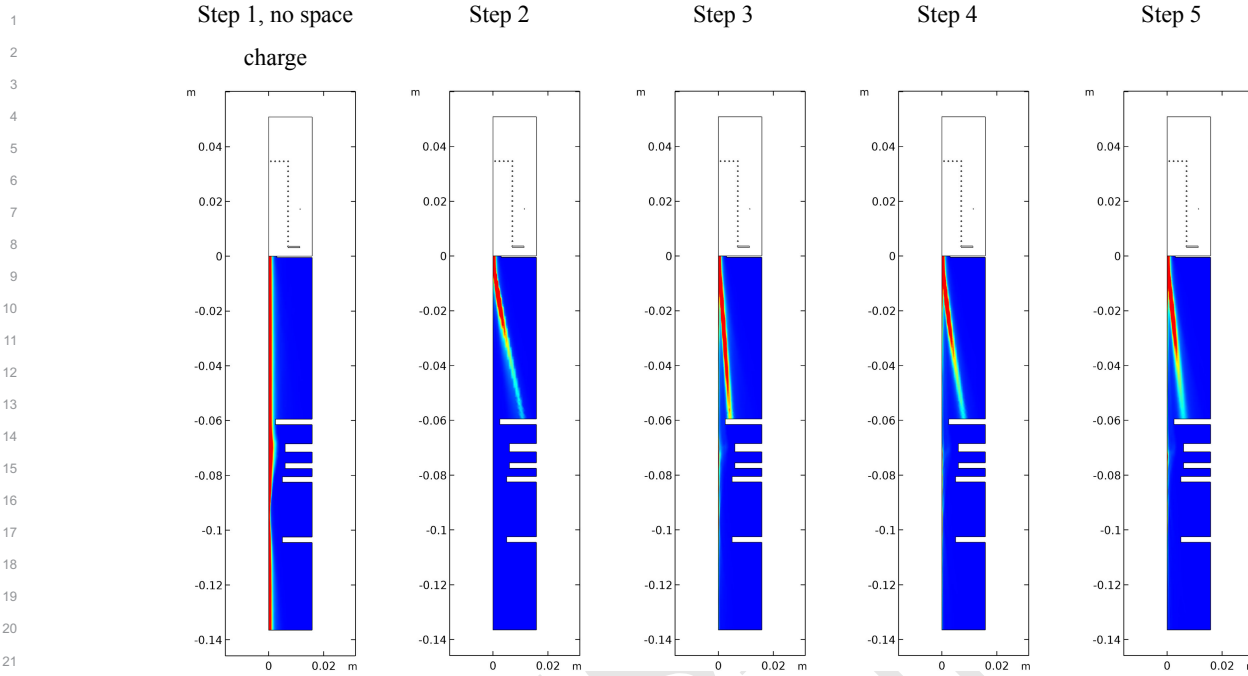


Figure 14: Explicit iteration steps to estimate the effect of coulomb forces by the ion space charge on the ion beam in the x - z plane through the electrostatic lens system.

H. Maximum gas pressure and filament current to prevent ion beam divergence

The positive ions in the ion beam repel each other, and thus the ion beam will diverge, however at low ion beam current densities this effect can be neglected. Using simulation modelling we have estimated from what ion beam current the coulomb forces become too dominant, and the ion beam will diverge too much to be able to obtain a neatly focused ion beam. Implicit coupling of coulomb forces with particle tracing is possible, but extremely calculation time consuming. Explicit coupling is less accurate and requires multiple iterations, but still is the way preferred. The effect of coulomb forces is implemented by a sequence of steps according the following scheme. The effect of these steps is shown in Figure 14.

1. Step 1: Space charge calculation without coulomb effect:
 - a) Electric potential calculation without ion space charge;
 - b) Ion trajectory calculation using electric potential without space charge.
2. Step 2: First order space charge:
 - a) Electric potential calculation with ion space charge from 1b;
 - b) Ion trajectory calculation using new electric potential.
3. Step N; ($N - 1$)th order space charge:
 - a) Electric potential calculation with ion space charge from previous order;
 - b) Ion trajectory calculation using new electric potential.

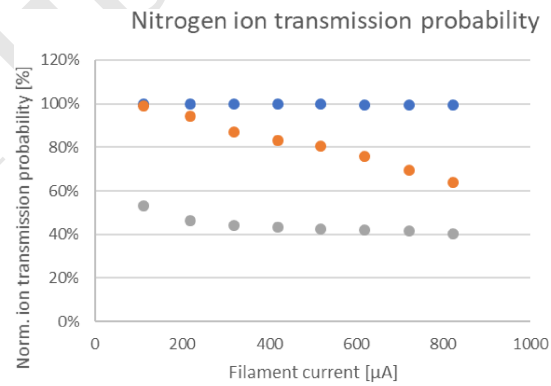


Figure 15: Ion transmission probability as nitrogen pressure and filament current for the SRS source.

4. Preferably an equilibrium state is found after N steps.

After five iteration steps the final position of the diverging ion beam is (almost) found. The density of the ion beam depends on gas pressure and filament current. The effect of both is shown in Figure 15, where it is clear that a gas pressure of 3×10^{-7} mbar does not lead to ion transmission loss due to beam divergence. At a gas pressure of 3×10^{-5} mbar we see ion transmission loss over all filament currents. At the intermediate pressure of 3×10^{-6} mbar we hardly see any loss at low filament currents up to 200 μ A, but increasing loss at higher filament currents. Based on this, we expect that no significant coulomb effects and a diverging ion beam in case of filament currents of 400 μ A combined with a gas pressure of 7.5×10^{-7} mbar. Therefore, continuing simulations have been performed up to these settings, and the effect of coulomb forces has been ignored. Furthermore,

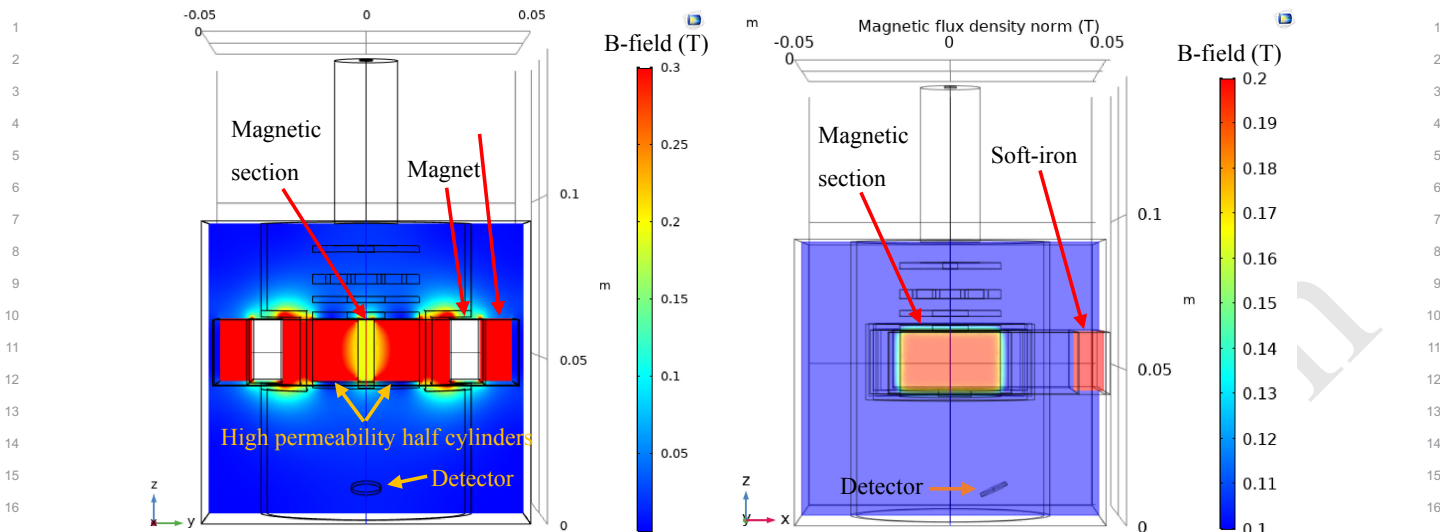


Figure 16: Left: Front-view of the MFIG model, without ion source, including magnetic B-field (maximized at 0.3 T). Right: Side-view of the MFIG model, including magnetic B-field in the magnetic section (maximized at 0.2 T).

based on these results it is recommended to use a maximum gas pressure of 7.5×10^{-7} mbar and a filament current of 400 μ A for the experimental validation.

I. Mass separation by magnetic ion beam deflection

The basic model set-up is shown in Figure 16. The ion source is not in the figure, but its location is on top of the white cylinder. The magnetic B -field, shows the magnetic section in the MFIG to be very homogeneous and confined. The magnetic field causes the ions to be deflected away from the centerline of the MFIG, and therefore the detector needs to be placed off-center, as shown in the right figure.

Magnetic mass discrimination by the magnetic field in the MFIG is shown in Figure 17. Ion beam trajectories in MFIG showing mass separation due to magnetic deflection. Only masses heavier than certain selectable weight will be detected, lighter ions will be deflected too much and will not hit the Faraday detector, where nitrogen, argon, krypton, and M100 gas are discriminated. Only M100 gas is detected by the faraday detector.

The magnets used are NdFeB Q-40-20-10-N magnets, bought from the company (Supermagnete), with a remanence of 1.29–1.32 T. The soft-iron bars are pure iron bars, supplied by Puron Metals. Puron Metals gives the relative permeability for initial, unannealed pure iron rods after cold-work in a range of 300–500. After annealing the cold-work effects can be neglected and the permeability increases to a range of 2000–20000, depending on the final metal grains. For the simulations the relative permeability was set to 5000. The magnetic saturation is very high at 2.15 T, so it is not expected that the magnetic field affects the permeability in the MFIG. The magnetic field in the magnetic section can be adjusted by adjusting the inter-magnet distance. Adjusting the magnetic flux in the magnet section allows for tuning the ion mass selectivity. Initial inter-magnet distance is set to

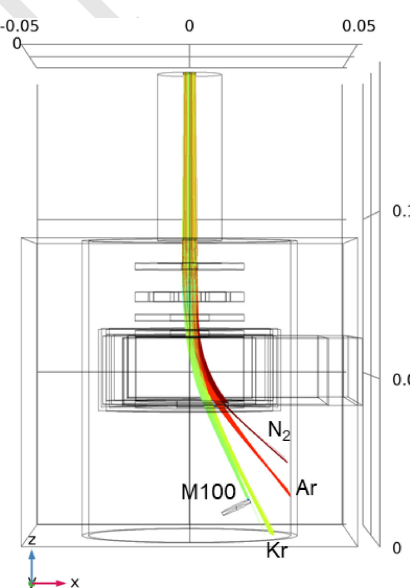


Figure 17: Ion beam trajectories in MFIG showing mass separation due to magnetic deflection. Only masses heavier than certain selectable weight will be detected, lighter ions will be deflected too much and will not hit the Faraday detector.

53 mm but can range from 41 to 63 mm. The magnetic flux density versus the inter-magnet distance is shown in Figure 18. The magnetic flux in the magnetic section was experimentally measured at 0.202 T. This value has been used for the experimental validation of the simulation model, and to set some of the unknown material's relative magnetic permeabilities.

Adjustment of the magnet spacing shifts the selectivity at both the lower and upper cut-off (Figure 19). The magnetic flux density shifts from 216 mT at 49 mm spacing down to 194 mT at 53 mm spacing, causing to shift the lower selectivity from 94 to 109 via 101 amu (from 49 to 51 via 51 mm

spacing), giving a delta of 15 amu. At the upper selectivity this delta has increased to 58 amu, ranging from 342 to 400 via 366 amu (from 49 to 53 via 51 mm). Based on the expected evaporation pressure of hydrocarbons with molecule masses above 300 amu we estimate that in all cases this upper sensitivity will be sufficient to detect all heavy contamination molecules.

To obtain this magnetic field homogeneously inside the MFIG magnetic section two half-cylinders of soft magnetic material Vacoperm® 100 are installed. The half-cylinders guide the magnetic field through the MFIG and divide the magnetic field homogeneously over the MFIG's magnetic section. Vacoperm® 100 material has been chosen for its excellent magnetic permeability of 3.5×10^5 at a magnetic flux of 0.3–0.5 T, with the material's saturation polarization at 0.74 T. The two half-cylinders are basically a cylinder with a length of 20 mm and a diameter of 34 mm diced in two parts with a saw width of 5 mm, creating a distance of 5 mm between the two parallel half-cylinders. All other metal parts are fabricated out of austenitic stainless steel 316, of which we estimated the magnetic properties negligible.

J. Scattering suppression to increase SNR

Ions lighter than the selected mass should not be detected

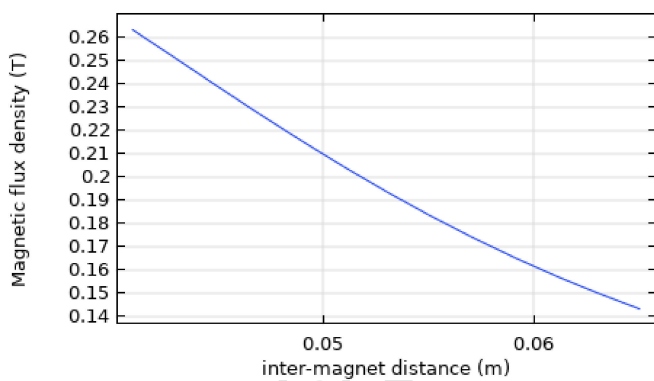


Figure 18: Magnetic flux density in magnet section as function of the inter-magnet distance between 41 and 63 mm.

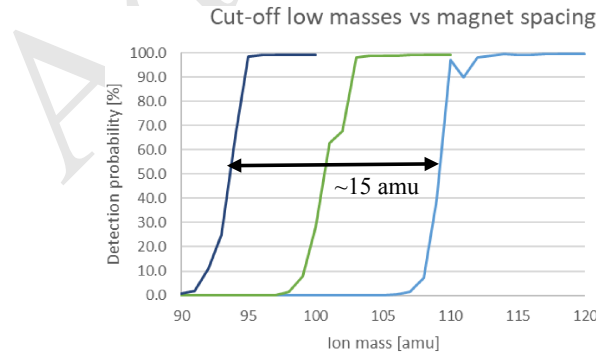


Figure 19: Effect of different inter-magnet distances on detection probability as function of ion mass. Changing the inter-magnet distance both affects the low mass cut-off (ion mass selectivity) (left) and the high mass cut-off (right).

by the detector. However, scattering of these light ions deflects the trajectories of these ions, and as a result they may end up at the detector, resulting in a background signal. To increase the SNR, this background signal should be minimized. Due to the much larger number of background gas, we aim at a SNR of 1×10^6 .

A rectangular aperture between the magnet section and the detector section is placed to prevent ions from process gases such as nitrogen and argon to enter the detector section (Figure 20). Krypton, whose mass is close to the sensitivity selection point of 100 amu, passes the rectangular aperture because it is estimated to be too critical to design the rectangular aperture length for stopping these ions.

Scattering of lighter background gases occur both in the magnet section and detector section. The chance that an ions scatters is estimated as [8]:

$$f_{\text{scat}} = 1 - e^{-\frac{s}{mfp}},$$

where s is the travel distance and mfp is the mean free path:

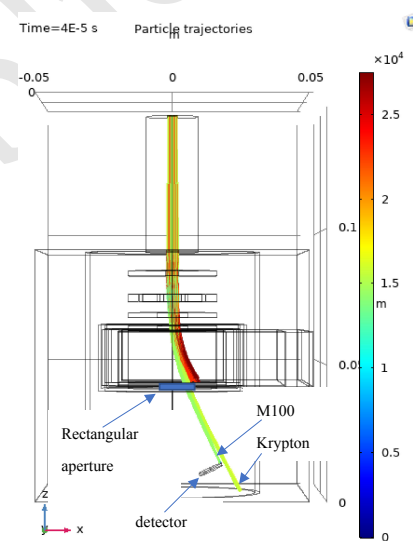
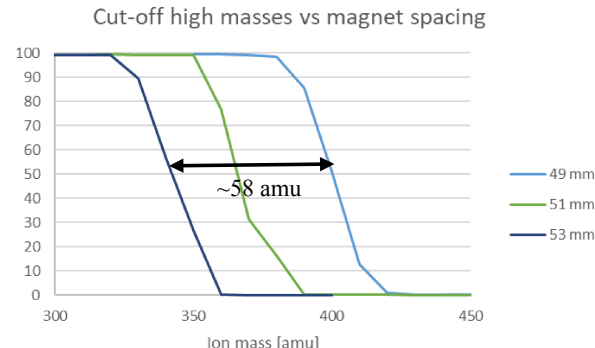


Figure 20: Simulation results show the effect of rectangular aperture (depicted as blue rectangle) dimensions on ions entering the detector section, where nitrogen and argon are efficiently blocked to minimize the background signal due to scattering.



$$mfp = \frac{1}{\pi(r_1 + r_2)^2 n},$$

where r_1 and r_2 are the kinetic radii of the ions and the gas molecules respectively, and n is the gas molecule number density. The kinetic radius of the ions is related to the kinetic radius of xenon ions (0.396 nm [11], mass 131 amu) via the following estimation with ion mass M :

$$r_1 = r_{\text{xenon}} \left(\frac{m_M}{m_{131}} \right)^{1/3}$$

The kinetic radii of the main process gases are taken from Refs. 11 and 12 and are listed in Table 3, and the calculated mean free paths of different light ions in selected process gases are listed in Table 4.

The gas molecule number density n is related to the gas pressure p and temperature T according to the ideal gas law:

$$n = \frac{p}{k_B T}.$$

For ion M100 (r_1 estimated at 0.362 nm) in nitrogen at 1.0×10^{-6} mbar the mean free path becomes 25.1 m. The chance of scattering $f_{\text{scat,magnet}}$ in the magnet section (length ~20 mm) equals 0.00080 and the chance of scattering $f_{\text{scat,detector}}$ in the detector section (length ~35 mm) becomes 0.0014.

1. Scattering in the magnet section

Scattering in the magnet section of any ion lighter than selectivity can contribute to the background detection current via two ways:

1. Single scattering: scattered ion leaves the magnetic section in the direction of the detector;
2. Multiple scattering: scattered ion leaves the magnetic section and is scattered again in the detector section in the direction of the detector. The chance of double scattering therefore is a product of $f_{\text{scat,magnet}}$ and $f_{\text{scat,detector}}$, which is equal to 1.1×10^{-6} . Furthermore, the first scatter should result in the ion leaving via the rectangular aperture, and the second scatter should result in the ion to hit the detector. Both chances reduce the double scatter chance of 1.1×10^{-6} significantly, and

Table 3: Kinetic radii of main process gases (Ar and Kr [11], and N₂ [12]).

	N ₂	Ar	Kr
Kinetic radius r_2	0.364 nm	0.340 nm	0.360 nm

Table 4: Calculated mean free paths of different light ions in common process gases at $p = 1 \times 10^{-6}$ mbar and $T = 300$ K.

Gas	Kinetic diameter (pm)	Mass (amu)	MFP in N ₂ (m)	MFP in Ar (m)	MFP in Kr (m)
Water	265	18	33.3	36.0	33.7
Nitrogen	364	28	24.9	26.6	25.1
Argon	340	40	26.6	28.5	26.9
Krypton	360	81	25.1	26.9	25.4

therefore we estimate background signal due to multiple scattering as negligible.

The chance for a scattered background gas ion the magnet site via the rectangular aperture and arrive at the detector is estimated to be

$$f_{\text{false,magnet,single scat}} = f_{\text{scat,magnet}} f_{\text{det,sight}}.$$

$f_{\text{det,sight}}$ is the chance the scattered ion arrives at the part of the detector in line of sight from scatter site through the rectangular aperture.

$$f_{\text{det,sight}} = \text{if}(\delta > \beta_L) * f_{\text{det}} \frac{(1 + \cos \delta) A_{\text{detector opening}} / 2}{A_{\text{half sphere}}}.$$

$$\delta = \sin^{-1} \left(\frac{\gamma - \beta_C}{\beta_R - \beta_C} \right);$$

$$\gamma = \tan^{-1} \left(\frac{x_{\text{ap}} - x}{z - z_{\text{ap}}} \right);$$

$$\beta_L = \tan^{-1} \left(\frac{x_L - x}{z - z_L} \right);$$

$$\beta_C = \tan^{-1} \left(\frac{x_C - x}{z - z_C} \right);$$

$$\beta_R = \tan^{-1} \left(\frac{x_R - x}{z - z_R} \right).$$

The geometry used for calculating $f_{\text{det,sight}}$ is shown in Figure 21. β is the angle between the vertical and the path between scatter site and detector (opening faraday cup). Three different angles of β apply: β_L , β_C , and β_R for the left side of the detector, the center of the detector, and the right side of the detector, respectively. γ is the angle between the vertical and the upper limit of the detector that is in sight of the scatter site. Angle δ is used to calculate the area of the detector opening that is in sight of the scatter site.

The lighter the ions the more they are deflected away from the aperture opening and single scattered ions can not be detected. So it is expected that heavier process gases (e.g., krypton) will lead to larger detection currents by scattering inside the magnet section than lighter process gases (e.g., nitrogen and argon) do.

2. Scattering in the detector section

The rectangular aperture is designed to block ions with a molecular weight below ~80 amu. Heavier ions will pass the rectangular aperture into the detector section, and scattering of these ions inside the detector section can contribute to the background detection current. The chance of detection of

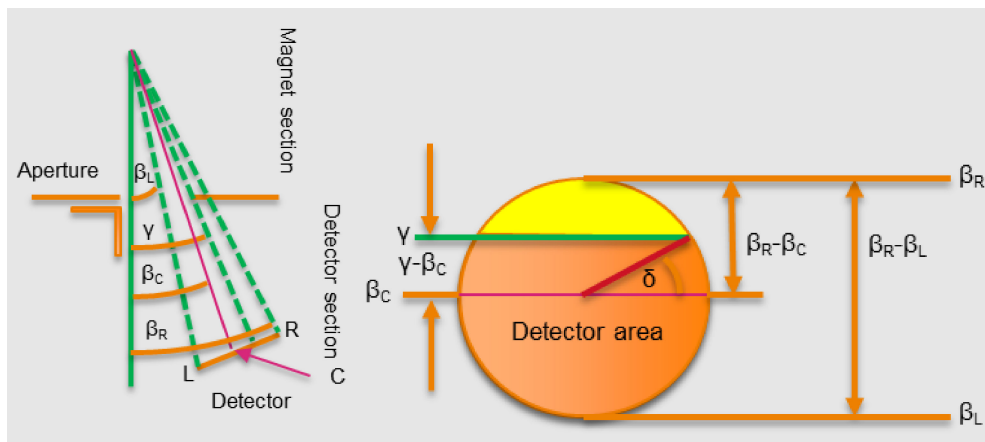


Figure 21: Schematic drawings showing the goniometry for the detection of single scattered ions from the scatter site in the magnet section. Left: side view showing the blocking of the detector by the rectangular aperture; Right: view of the detector area (faraday cup opening) with active detector area due to the blocking of the rectangular aperture.

Table 5: Calculated scatter currents for different process gases, compared to calculated partial pressures, at which the detector signal is equal to the scatter signal, for different contamination masses. Values valid for gas pressure of 1×10^{-6} mbar and temperature of 300 K.

Process gas	I_{scatter} (A)	$p_{\text{M100}} I_M = I_{\text{scat}}$ (mbar)	$p_{\text{M150}} I_M = I_{\text{scat}}$ (mbar)	$p_{\text{M200}} I_M = I_{\text{scat}}$ (mbar)
Krypton	2.7×10^{-13}	6.6×10^{-12}	5.0×10^{-12}	4.1×10^{-12}
Argon	7.1×10^{-15}	1.7×10^{-13}	1.3×10^{-13}	1.1×10^{-13}
Nitrogen	5.0×10^{-15}	1.2×10^{-13}	9.3×10^{-14}	7.7×10^{-14}

false positives due to scattering in the detector section is estimated as:

$$f_{\text{false,detector}} = f_{\text{scat,detector}} f_{\text{det.}}$$

When we compare scattering in the detection section to scattering in the magnet section we see a closer vicinity of the scattered ion to the detector, leading to an increase of $f_{\text{det.}}$. Therefore, if scattering in the detector section occurs, it will have a larger effect on the background signal than scattering in the magnet section.

3. Simulation results on background signal due to scattering

The ion trajectories have been modelled in COMSOL using particle tracing, with the scattering equations implemented. Integrating over the particle trajectories we can estimate the total scatter chances, and thus scatter signal, per process gas for a certain gas pressure and temperature. Table 5 shows the background detection currents of different process gases and the partial pressures of M100, M150, and M200 contaminations where the contamination signal equals the scatter signal. For these calculations gas pressure was set to 1×10^{-6} mbar and the temperature was 300 K.

It is obvious krypton leads to much larger scatter currents than argon ($38\times$) and nitrogen ($54\times$) because krypton ions will pass the rectangular aperture into the detection section whereas argon and nitrogen ions are blocked by the rectangular aperture, and thus do not scatter in the detector section. For illustration, the scatter current of krypton from the mag-

net section is 9.3×10^{-15} A and from the detector section this is 2.6×10^{-13} A. Thus, 96% of the scatter current of krypton is from the detector section, only 3.4% is from the magnet section. Elimination of the scatter current from the detector section is very beneficial for detecting low contamination partial pressures. Therefore, it is easier to detect much lower contamination levels when using nitrogen or argon as process gas. For detecting contamination partial pressures in the 1.0×10^{-13} mbar region it is advised to use nitrogen or argon as process gas. The aim was to achieve SNR of 1×10^6 . According to FEM simulations this is feasible for argon and nitrogen as background gases, krypton as background gas allows SNR of 1.5×10^5 .

Due to the increasing ion size at heavier contaminations, lower partial pressures of heavier contaminations are detected at identical detection current.

III. EXPERIMENTAL EVALUATION

Several key performance figures of MFIG had been tested and evaluated in a laboratory environment. The laboratory test setup is depicted in Figures 22 and 23.

A. Mass selectivity

MFIG is mass selective. Ions are deflected both by the electrostatic lens and by the magnetic field. Contrary to the electrostatic lens, the deflection angle in the magnetic field section depends on the ion's mass. Only the electrostatic lenses are used to select the masses. The magnetic field

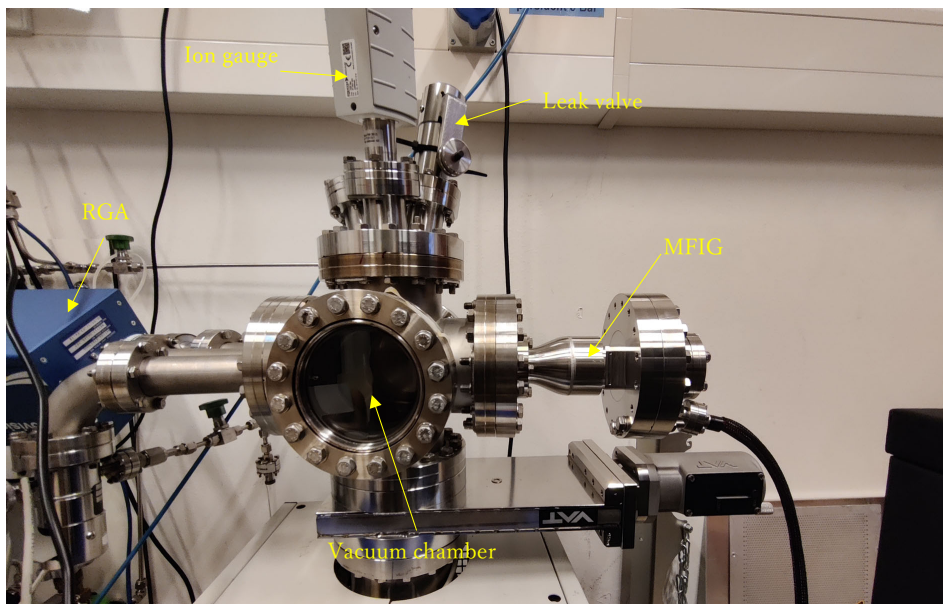


Figure 22: Vacuum test setup with RGA attached on left side, MFIG attached on right side (in build-up phase: no magnets nor Faraday detector attached).

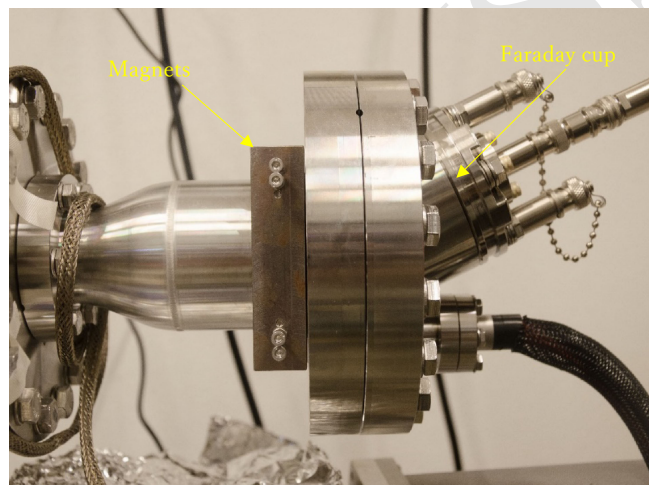


Figure 23: MFIG with magnet and Faraday cup installed.

cannot be tuned during operation. The Faraday cup is positioned such that only ions within a certain mass range can be detected, as shown in [Figure 24](#). Contrary to a state-of-the-art RGA, MFIG is not equipped with an additional secondary electron multiplier (SEM) although a SEM could be added to a future MFIG design. Therefore, MFIG can only operate in Faraday mode.

In [Figure 25](#) we have measured the ion current detected by MFIG for three test gasses. N₂, xenon, and krypton. We have varied the electrostatic [north-south (NS)-dipole] voltage. As a result, we are shifting the masses of the Xe, Kr, and N₂ ions in and out of the mass range of MFIG.

The working principle of the MFIG is based on the fact that ions that move in a magnetic field are dispersed by a magnetic field. If ions with the same kinetic energy are present in the magnetic field, low mass ions are dispersed more than high mass ions. The dispersion distance depends on ion mass, ion charge, kinetic energy of the ion and the magnetic field:

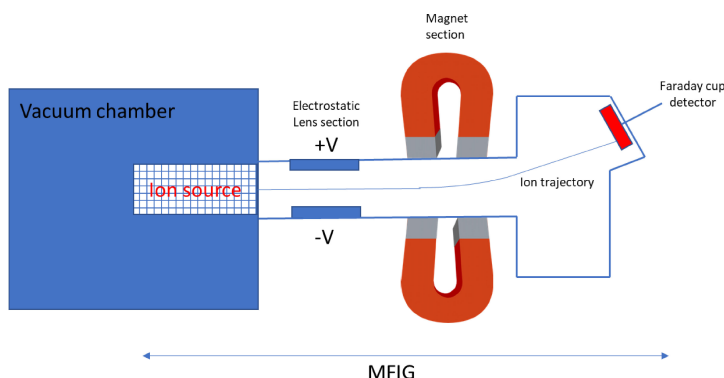


Figure 24: Block diagram of MFIG.

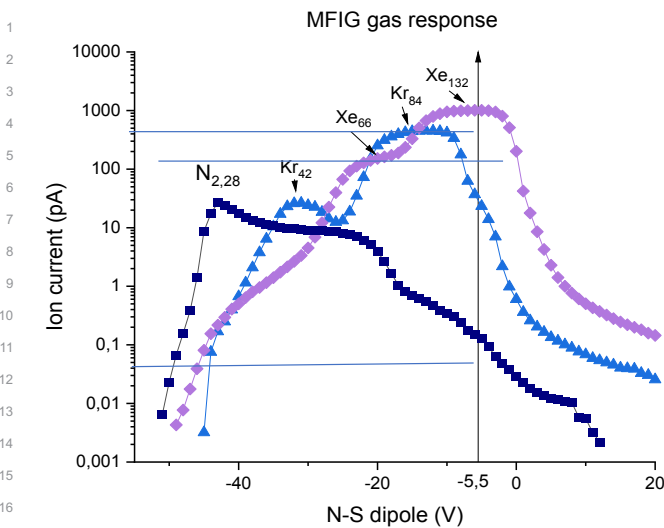


Figure 25: MFIG ion current for krypton, xenon, and nitrogen as function of electrostatic (NS-dipole) voltage.

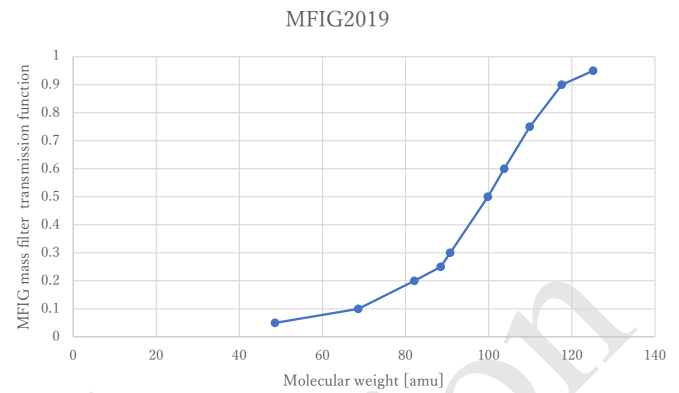


Figure 27: MFIG mass filter transmission function for MFIG set at 100 amu lower mass cut-off.

of the peak height (for N₂, Kr, and Xe) against $1/\sqrt{M}$ —blue/red lines in Figure 26. The top blue line in Figure 26 represents the lower cut-off limit. Here, low mass and high mass ions are separated. The bottom red line is the result of the finite detector size. For large negative NS-dipole settings, the deflection of the high mass ions is more than the detector size and these masses fall outside the detector.

Based on this curve we can determine which NS dipole voltage is needed to set the mass selectivity to a desired mass. From this plot, we deduce that an electrostatic voltage of around -5.5 V gives a lower mass cut-off of around 100 amu. For this setting, nitrogen is suppressed by a factor of ~10000 compared to xenon-132, see Figure 25.

B. Filter function

MFIG is a mass filtered ion gauge, this means that ideally only masses in a selected mass range are detected. The filter function determines how strongly masses outside of the mass range are suppressed. This is important for low concentrations measurements of e.g., heavy hydrocarbons without being swamped by residual water partial pressure. If the filter function is steeper, the selection of masses works better.

Shown in Figure 27 is the filter function of MFIG. The mass filter transmission function of MFIG is calculated by using the data from Figure 26.

C. Lower detection limit

The lower detection limit is determined by the noise performance of MFIG, when at ultra high vacuum (UHV) conditions. The noise level is determined by the noise level of our current amplifier, but also by the noise level of our anode current control circuitry.

The lower detection limit was determined by using a mixture of Xe in nitrogen. Initially we made use of three mix ratios: 1, 0.01, and 0.0001%. The mixture was made in a separate mixing chamber and fed into the measurement chamber using a leak valve. The results are depicted in Figure 28.

It turned out that we could not go lower in mix ratio than 1%. For a lower Xe in N₂ ratio, the contribution of N₂ dominates the MFIG signal. That is the reason why the red

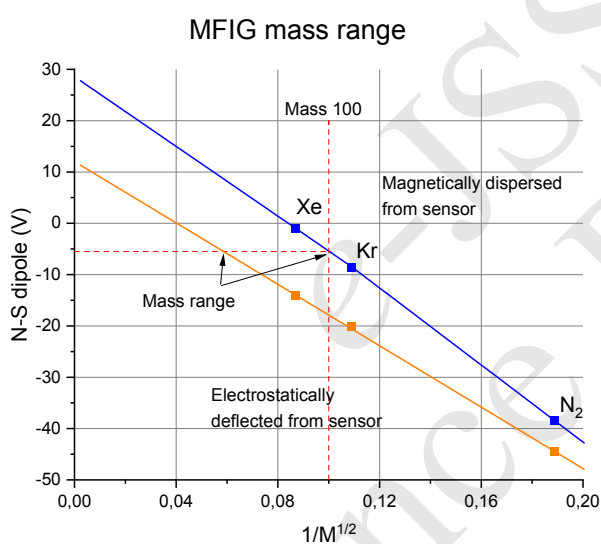


Figure 26: Electrostatic (NS-dipole) voltages for which ion current is at 50% of its maximum for Xe, Kr, and N₂, plotted vs. $1/\sqrt{M}$. Red lines show fits of the NS-dipole voltage at 50% of the peak height (for N₂, Kr, and Xe) against $1/\sqrt{M}$. Black lines at NS voltage of -8 V gives lower mass cut-off at 100 amu (crossing of black line with top red fit line).

$$dx \propto \frac{B\sqrt{q}}{\sqrt{IE M}}.$$

Here, dx is a dispersion distance, B is a magnetic field, q is ion charge, IE is a kinetic energy of ions (ion energy), and M is an ion mass. The electrostatic displacement is proportional to the NS-dipole voltage.

The graphs in Figure 25 can be further analyzed. In Figure 26, we have plotted the electrostatic (NS-dipole) voltage for which the ion currents in Figure 25 for N₂, Kr, and Xe are at 50% of their maximum value (blue dots and red hexagons). Linear fits were made of the NS dipole voltage at 50%

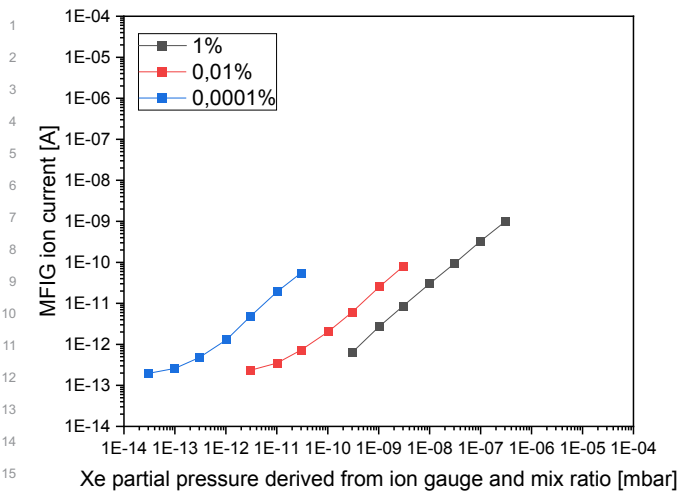


Figure 28: Ion current detected by MFIG for mixtures of Xe in N₂.

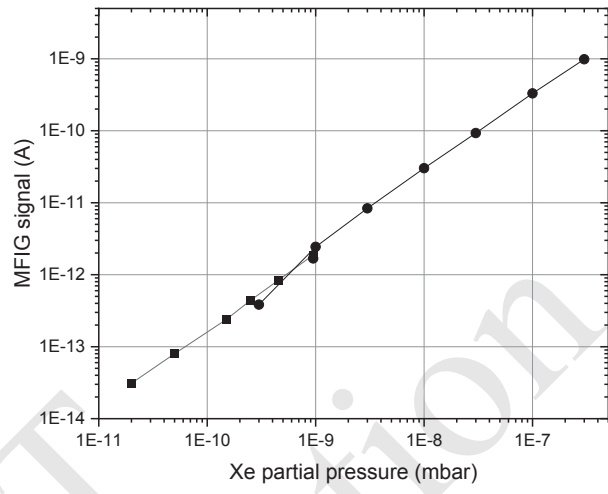


Figure 30: Ion current detected by MFIG for mixtures of 1% Xe in N₂. The signal consists of about 83% Xe and 17% N₂ (see Figure 29).



Figure 29: Ion current calculated for MFIG for a mixture of 1% Xe in N₂. Separately the contribution of N₂ and Xe to the MFIG signal is plotted vs. Xe partial pressure.

and blue curves in Figure 28 are not aligned with the black curve. Nitrogen is suppressed compared to xenon by approximately a factor 1000, however this is insufficient to eliminate the 10000- and 1000000-fold higher partial pressure of nitrogen in the red and blue measurement curves, respectively. Therefore, the mix ratios below 1% cannot be used to measure the lower detection limit. Optimization has been in progress to overcome this issue.

For a mixture of 1% Xe in N₂, Figure 29 shows the contribution of Xe and N₂ to the total MFIG signal. For this mix ratio, Xe still dominates the MFIG response.

It can be seen in Figure 28 that for mixtures of 0.01 and 0.0001%, the curves level off at a MFIG ion current of $\sim 1 \times 10^{-13}$ A. Around this current level, we are limited by noise from our current detector for the used settings (integration time of 20 ms and large dynamic range). For a mixture of 1% levels, MFIG current lower than 1×10^{-12} A could not be measured since gas mixture pressure is set using a needle valve in combination with a total pressure sensor and we could not lower the gas mixture pressure below the background pressure of the system of $\sim 5 \times 10^{-8}$ mbar (without bake out).

Optimization of the current detector settings resulted in a lower noise level in a follow-up experiment. The lower detection limit with these optimized noise settings was then further studied using the 1% Xe in nitrogen mixture gas prior to a bake-out of the system which resulted in a background pressure of 5×10^{-9} mbar. With MFIG the lower detection limit is now around 2×10^{-11} mbar Xe as can be seen in Figure 30.

D. Faster detection

The key performance indicator (KPI) of this sensor is that the sensor will be faster ($\times 100$) than the state-of-the-art RGA for real-time sensitive measurements. To measure the KPI we have performed a test in a vacuum setup to which we have attached the MFIG and a state-of-the-art RGA. A MKS Microvision 2 RGA was selected as a state-of-the-art. The RGA was used in Faraday cup mode. The SEM was not used, since MFIG by design has no SEM built in. In an enhanced MFIG version, a SEM could be implemented. Addition of a SEM increases the cost of MFIG and reduces the noise level by a factor 100–1000.

A mixture of 1% Xe in N₂ was made in a mixing chamber. Subsequently, the Xe/N₂ gas mixture was introduced in the measurement chamber through a leak valve. The background pressure of the turbo-molecular pumped vacuum system after bake-out was 5.0×10^{-9} mbar. We introduced 1% Xe in N₂ into the system for various pressure levels as shown in Table 6. With both the MFIG and RGA we measured whether each of them could detect the increase in Xe pressure.

With the RGA in Faraday cup mode with 1 point per amu, Xe is only detectable in speed mode 8 (eight speed modes available, mode 1: fastest, mode 8: slowest) and only if the Xe partial pressure is at a level of 2.5×10^{-10} mbar and above. If the exact mass of the contaminant is unknown and the mass range of 100–200 amu needs to be scanned, it takes the RGA 126 s, while MFIG only needs 1 s to detect Xe. There-

1 **Table 6:** Overview KPI measurement results.

	total pressure (mbar)	partial Xe corrected background (mbar)	partial N ₂ corrected background (gas inlet) (mbar)	MFIG		RGA		
	(mbar)	(mbar)	(mbar)	signal (pA)	time (s)	time (s)	signal (mbar)	speed settings
Background	5.0×10^{-9}	0	0	0.045			-	
Background	7.0×10^{-9}	2.0×10^{-11}	1.98×10^{-9}	0.065	1	126	-	8
Background	1.0×10^{-8}	5.0×10^{-11}	4.95×10^{-9}	0.135	1	126	-	8
Background	3.0×10^{-8}	2.5×10^{-10}	2.48×10^{-8}	0.41	1	126	2.0×10^{-10}	8

fore, MFIG is in this situation 126 times faster than the state-of-the-art RGA. At the same time, we see that MFIG can already detect Xe at a partial pressure of 2×10^{-11} mbar, so MFIG is a factor 10 more sensitive than the state-of-the-art RGA.

IV. CONCLUSIONS

MFIG is a new metrology tool that can detect “short” bursts of contamination starting from a mass heavier than typically 100 amu (voltage selectable). When these contamination bursts have been detected the operator or the system is immediately notified and either the operator or system can take next steps, allowing for cycle-time reduction in case of a contamination event and thus preventing further yield loss.

The KPI of the high vacuum use case MFIG is to detect a change in VOC and AMC partial pressure in a vacuum system at an unprecedented time resolution, relevant for electron microscopy-based metrology and inspection tools and extreme ultraviolet lithography systems. We have demonstrated that MFIG is more than 100 times faster than the state-of-the-art RGA both running in Faraday mode.

At a Xe partial pressure of 2.5×10^{-10} mbar MFIG only needs 1 s to detect Xe. MFIG is in this situation 126 times faster than the state-of-the-art RGA. At the same time, we see that MFIG can already detect Xe at a partial pressure of 2×10^{-11} mbar, a factor 10 lower than the RGA, which is a factor 10 more sensitive.

Acknowledgement

This project has received funding from the ECSEL Joint Undertaking (JU) under grant agreement No. 826589. The JU receives support from the European Union’s Horizon 2020 research and innovation programme and France, Germany, Austria, Italy, Sweden, Netherlands, Belgium, Hungary, Romania, Israel.

Note

This paper was presented at the 22nd International Vacuum Congress (IVC-22), Sapporo Convention Center, Sapporo, Japan, 11-16 September, 2022.

References

- [1] D. Maas, P. Muilwijk, M. van Putten, F. de Graaf, O. Kievit, P. Boerboom, and N. B. Koster, *Proc. SPIE* **10145**, 1014521 (2017).
- [2] RGA Ion Source, Hiden Analytical Ltd. (<https://www.hidenanalytical.com/wp-content/uploads/2022/02/RGA-Ion-Source-Assembly-new-format.pdf>) (Last accessed: July 31, 2023).
- [3] J. Orloff, in: *Handbook of Charged Particle Optics*, 2nd ed., edited by J. Orloff (CRC Press, 2008) pp. 5–6.
- [4] C. R. Crowell, *Solid-State Electron.* **8**, 395 (1965).
- [5] J. M. Bernhard, *Work Function Study of Iridium Oxide and Molybdenum Using UPS and Simultaneous Fowler-Nordheim I-V Plots with Field Emission Energy Distributions* (University of North Texas, Denton, 1999).
- [6] Application Notes, *Bayard-Alpert Gauge Filaments: Tungsten or Thorium?*, Stanford Research Systems, Inc. (<https://www.thinksrs.com/downloads/pdfs/applicationnotes/IG1filamentsapp.pdf>) (Last accessed: July 31, 2023).
- [7] H. Kawano, *Prog. Surf. Sci.* **83**, 1 (2008).
- [8] M. A. Lieberman and A. J. Lichtenberg, *Principles of Plasma Discharges and Materials Processing*, 2nd ed. (Wiley, Hoboken, NJ, 2005).
- [9] S. F. Biagi, MagBoltz ver. 8.97 database (www.lxcat.net) (Last accessed: July 31, 2023).
- [10] G. D. Shirkov, *Nucl. Instrum. Methods Phys. Res. A* **391**, 117 (1997).
- [11] D. W. Breck, *Zeolite Molecular Sieves: Structure, Chemistry, and Use* (Wiley, New York, 1974).
- [12] A. F. Ismail, K. Khulbe, and T. Matsuura, *Gas Separation Membranes: Polymeric and Inorganic* (Springer Cham, 2015).



All articles published on e-J. Surf. Sci. Nanotechnol. are licensed under the Creative Commons Attribution 4.0 International (CC BY 4.0). You are free to copy and redistribute articles in any medium or format and also free to remix, transform, and build upon articles for any purpose (including a commercial use) as long as you give appropriate credit to the original source and provide a link to the Creative Commons (CC) license. If you modify the material, you must indicate changes in a proper way.

Copyright: ©2023 The author(s)

Published by The Japan Society of Vacuum and Surface Science